Received 3 February 2024; revised 12 May 2024; accepted 28 May 2024.
Date of publication 31 May 2024; date of current version 7 June 2024.

Digital Object Identifier 10.1109/OJUFFC.2024.3408138

Theoretical Validation of a Single-Channel Air-Coupled PMUT With Multi-Frequency Operation for Compressed 3D Spatial Sensing

TINGZHONG XU[1], ZHONGJIE ZHANG[1,2], RODRIGO TUMOLIN ROCHA[1], LIANG ZENG[2], AND CHUNLEI XU[3]

[1]Silicon Austria Labs GmbH, 9524 Villach, Austria
[2]School of Mechanical Engineering, Xi'an Jiaotong University, Xi'an, Shaanxi 710049, China
[3]Silicon Austria Labs GmbH, 4040 Linz, Austria

(Tingzhong Xu and Zhongjie Zhang contributed equally to this work.) CORRESPONDING AUTHORS:
T. XU (tingzhong.xu@silicon-austria.com), L. ZENG (liangzeng@mail.xjtu.edu.cn), and C. XU (chunlei.Xu@silicon-austria.com)

This work was supported in part by the Silicon Austria Labs (SAL) GmbH (Internal Research Budget: COMPOSML), owned by the Republic of Austria, under Grant 707700; in part by the Styrian Business Promotion Agency (SFG); in part by the Federal State of Carinthia; in part by the Upper Austrian Research (UAR); and in part by Austrian Association for the Electric and Electronics Industry (FEEI).

ABSTRACT This paper proposes a new 3D spatial sensing approach via compressed sensing (CS) by using a single-channel air-coupled piezoelectric micromachined ultrasonic transducer (PMUT) operated with multi-frequency. Our study focuses on a single-channel transducer with a PMUT array composed of several diaphragms with different radius sizes. It is known that small variations in the radius size can cause distinct transmission signals of all diaphragms that are excited by the same excitation signal. In this way, the acoustic field distribution of a region of interest (ROI) can be distorted especially in the direction perpendicular to the wave propagation, which could help to obtain more distinctive information about the scatterers at different locations in any 3D ROI. Therefore, a compressed 3D spatial sensing approach is proposed and used for acquiring measurements of the designed single-channel transducer. The information of any object in a 3D ROI can be mapped onto a collection of basis functions constructed via the nearly mutual orthogonal echo signals from all scatterers in the ROI. Furthermore, the proposed approach is verified with simulated acoustic measurements obtained from the established PMUT equivalent circuit model and the K-Wave acoustic propagation model via an obstacle-sensing application. Based on the sparsity nature of objects in the ROI, the reconstruction of 2D/3D images of objects can be accomplished via a CS-based algorithm. The obtained image reconstruction results show that the proposed approach allows not only for detecting localization but also for reconstructing descriptive features of an object.

INDEX TERMS Air-coupled ultrasound, compressive sensing, piezoelectric micromachined ultrasonic transducer (PMUT), 3D spatial sensing, ultrasound imaging.

I. INTRODUCTION

ULTRASOUND imaging has attracted widely attention and achieved tremendous improvements in the last decades. Due to its versatile and non-invasive properties, ultrasound imaging techniques can provide real-time, quantitative physical and anatomical information, and further facilitate to capture of meticulous information on objects in certain applications such as structural cracks, pathological tissues, and obstacles. Due to the penetration capability, safety (non-radiation), and economic efficiency properties of ultrasound, the development of ultrasound imaging benefits other ultrasound domains, especially for the ultrasonic testing (UT) technology employed in a wide variety of applications from nondestructive testing [1], [2], medical diagnosis [3], [4] to communication navigation [5], [6].

Nowadays, several ultrasound imaging approaches have been used for object identification, localization, and quantification, such as the delay-and-sum (DAS) beamforming

[7], [8], [9], the multiple signal classification (MUSIC) algorithm [10], [11], and the time domain topological energy (TDTE) [12], [13]. However, most ultrasound imaging approaches still mainly focus on dealing with the two-dimensional (2D) imaging of a region of interest (ROI). To achieve comprehensive three-dimensional (3D) imaging of an ROI and effectively characterize 3D objects, including shapes and volumes, it is necessary to mechanically or electrically scan the ultrasonic beam, such as with phased array technology. This approach allows for the collection of additional measurements of objects at various positions and angles. As demonstrated in [14], using a rotatable linear array, a C-Mode ultrasonic tomography is used to perform imaging of a breast model, allowing the size and location of the mass to be recognized. As reported in [15], transmit beamforming is applied to obtain a narrow beam, and a mechanical moving sensor array is used to scan the sample, which can generate the B-mode and C-mode images with high resolution for characterizing objects. However, achieving the transmit beamforming system requires additional circuitry to independently perform the delay control, leading to a more complex design of a sonar sensing system. In addition, mechanical scanning is an exhausting and time-consuming process to obtain a large amount of experimental data for reconstructing the desired 3D images of objects, which makes designing an imaging system with a high frame rate for high-quality images very challenging. Therefore, it becomes more urgent for the sensing scenarios, such as 3D imaging, and 3D spatial sensing, to find other suitable approaches that produce compressed data during the sensing to reduce the amount of required measurements for 3D imaging reconstruction.

In recent studies, compressed sensing (CS) [16], [17] provides one promising solution to address the current limitation of 3D ultrasound imaging. It states that, by carefully selecting a sparse representation base and a suitable sampling strategy, the measurement acquisition procedure can be accelerated with the reduced measurement volume, while still the essential information of the target signal can be guaranteed accurately reconstructed. So far, CS has been employed in various applications, including communication systems and networks [18], medical imaging [19], and seismology [20]. In particular, CS-based measurement acquisition with single sensors has demonstrated the great potential of the CS-based imaging approach. Duarte et.al. [21] proposed a single-pixel camera, which uses a single photodetector with an adjustable mask to reconstruct images. By projecting an image onto the photodetector through randomized mask patterns, they successfully reconstructed the ground-truth image from a few measurements less than the total number of image pixels. Similarly, in the field of ultrasound imaging, Kruizinga et al. [22] demonstrated a coding mask embedded in a single ultrasound sensor to break the phase uniformity of the ultrasound wave in an ROI, where each pixel reflects a unique temporal echo signal. Thus, the 3D spatial information of an object can be projected onto a set of incoherent basis constructed by coding masks based on temporal echo signals, and the 3D image reconstruction of an object can be achieved via reconstruction algorithms developed in CS. Compared to the traditional 3D ultrasound imaging approach of mechanically moving imaging systems, the CS-based 3D imaging approach can significantly reduce measurement volume and measurement acquisition time. Additionally, it also benefits by reducing the complexity of hardware system implementation and with less additional cost added to the single ultrasound sensor. However, the coding mask introduces other problems to the ultrasound sensing system. For instance, the coding mask may cause multiple reflections inside the mask before the ultrasound waves reach the objects, which results in significant energy loss. In addition, the traditional bulk ultrasound sensor used in [22] usually has poor impedance matching due to the thickness vibration mode in fluid media, which makes the coding mask-based imaging approach not suitable for air-coupled sensing applications.

However, with the development of micro-electromechanical systems (MEMS) technology, piezoelectric micromachined ultrasonic transducers (PMUT) have become an excellent solution for improving the transmission efficiency of the system, especially for the fluid-coupled applications compared to the traditional bulk ultrasonic sensors. PMUT transmits and receives ultrasonic through a curved film in flexural vibration mode (d_{31}), yielding enhanced acoustic impedance matching between the sensor cell and the air-coupling [23], [24], [25]. With the current lithography technology, the resonance frequency of the PMUT cell can be easily tuned by adjusting their 2D patterns. Furthermore, PMUT possesses several advantages over traditional ultrasonic sensors in terms of circuit integration, low driving voltage, and high receiving sensitivity [26], [27].

To break the limitation of 3D ultrasound imaging and utilize the benefits of PMUT in fluid media or air-coupled sensing applications, this paper proposes a new 3D spatial sensing approach throughout compressed sensing by using a single-channel air-coupled PMUT operated with multi-frequency. Firstly, a new sensor design is presented in this paper for 3D spatial sensing in air, where a PMUT array is composed of several cells with different radius sizes. A single channel is utilized to control all the cells by applying the same excitation signal to all of them simultaneously. The variance of radii of cells results in distinct frequency responses between each other, which causes the distorted distribution of the acoustic field in the entire space of ROI. This could help remove ambiguous echoes from scatters at different locations in an image plane of ROI perpendicular to the wave propagation direction. Secondly, following the principle of CS, a compressed 3D spatial sensing approach is demonstrated with the designed single-channel sensor, where the information of any 3D object in the ROI can be mapped onto a collection of non-coherent basis functions constructed via the nearly mutual orthogonal echo signals from all scatters in the 3D ROI. Finally, based on the sparsity nature of objects in the ROI, the 3D image reconstruction of objects is accomplished by algorithms used to solve the CS problems.

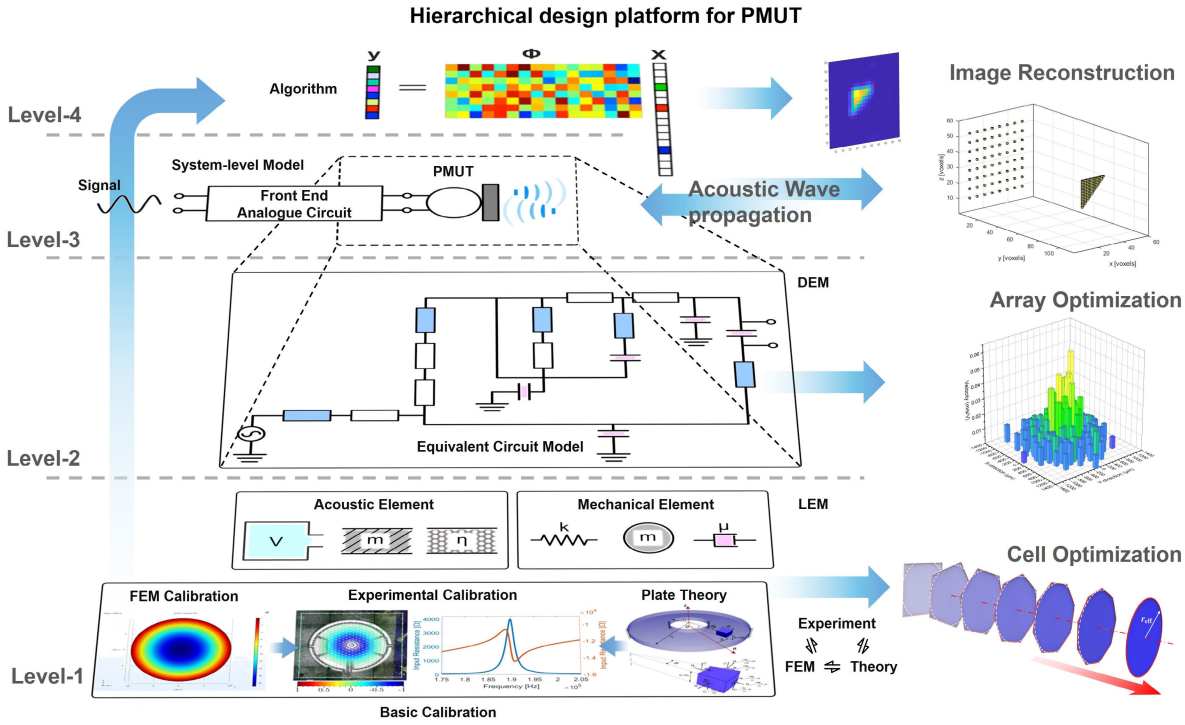

FIGURE 1. Schematic of the hierarchical design platform employed for a comprehensive development of a PMUT-based system.

Compared to the coding mask-based 3D imaging method, the proposed method utilizes a PMUT array and can avoid the coding mask causing unnecessary multiple reflections, which can improve energy transmission efficiency. The control circuit for a single-channel sensor simplifies the system hardware implementation compared to the traditional delay control-based system implementation and further reduces the total cost of the sensor system. The CS-based data acquisition process used for building the sparse representation matrix via echo signals has not only overcome the time-consuming process of pixel-wise scanning in traditional methods but also can achieve a significantly reduced number of measurements. In addition, this paper has established a time-domain equivalent circuit model based on a PMUT array simulation platform. The acoustic measurements of the proposed method are obtained through the combination of the platform for PMUT transmission and reception, and the K-Wave acoustic propagation model [28], [29], [30]. The developed simulation platform has significantly improved the efficiency of the time domain simulation for any studies on PMUT arrays, building up a foundation for the succeeding system optimization and other researches on PMUT applications.

The remainder of the paper is organized as follows. Section II provides a thorough explanation of the hierarchical design platform employed in the PMUT system, illustrating its integration with a sophisticated compressed 3D spatial sensing algorithm. In Section III, the PMUT equivalent circuit model is established in the time domain. The details of the proposed compressed 3D spatial sensing method are presented in Section IV. Section V describes the simulation setup and verifies the effectiveness of the established PMUT time domain-based simulation platform. Furthermore, the study and the validation of our proposed method are carried out with simulated measurements on 2D/3D objects spatial sensing, and corresponding analysis results are presented in Section VI. Finally, conclusions are drawn in Section VII.

II. SYSTEM LEVEL PARADIGM

During the standard operations of PMUTs, multiple physical domains including fluid dynamics, mechanics, and electronics are coupled together. An accurate and efficient collaborative design taking multiple factors into account is critical to upgrade the performance of the entire system. To address this challenge, we developed a system-level simulation platform for the hierarchical design of PMUT-based systems, enabling comprehensive designing and optimization of the entire system. Figure 1 illustrates the technical roadmap of the proposed platform. This design platform mainly consists of four levels, given as

- Level 1 focuses on the modeling of a single PMUT cell. This segment relies on classical plate vibration theory and theoretical acoustics, allowing analytical solutions [31], [32]. Additionally, finite element method (FEM) simulations can be performed using commercial software like COMSOL or ANSYS, either calibrated based on experiments. This approach guarantees the

versatility and accuracy of the proposed PMUT simulation platform. Subsequently, a lumped element model (LEM) of the PMUT cell can be established, consolidating all physical parameters into electrical ones;

- Level 2 relies on an equivalent circuit model formulated for PMUT array design and optimization. The lumped element parameters obtained from level 1 are applied to construct the distributed element model (DEM) of the array. This significantly diminishes the computational load for simulating a large array over a broad frequency range compared to the finite element method (FEM). Such an approach is proved particularly beneficial in forecasting the performance of extensive PMUT arrays intended for liquid-coupled applications [24], [25], [26], [27];
- Level 3 integrates the electrical model of a PMUT with the front-end analog circuits, conducting a multiple-domain coupled simulation to obtain the electrical output signal from the hardware system, serving as input for level 4;
- Level 4 is grounded in the previously mentioned hardware systems modeling. It entails selecting appropriate algorithms according to the characteristics of the hardware system to fully leverage its advantages and optimize the algorithms accordingly.

Note that the first three levels are focused on the hardware, as described in Sec. III, and level 4 is related to the signal processing techniques and algorithms illustrated in Sec. IV.

This platform does not only significantly increase the computation efficiency when accounting for any large PMUT array, but also establishes a coupling relationship among the multi-physics domains, directly building the relationship between the structural design of the PMUT and the final output of the whole system. In other words, it has the potential to yield an optimization guideline of the whole system from scratch. The modular design approach of this platform enables the combination of individual design modules based on specific analysis scenarios, achieving the most economically efficient approach while ensuring design requirements are met.

Compared to FEM and pure numerical simulation method, it is easier to find a clear optimization guideline from the proposed equation-based semi-analytical system, which can standardize all parameters as electrical variables with a uniform format. It does not only facilitate a systematic approach to system design but also expands the possibilities for employing more methods from electrical network theory. In addition, it enables sophisticated system analyses exemplified by the utilization of circuit simulation software such as Keysight ADS.

III. HARDWARE SYSTEM PARADIGM

A. PMUT MODELING

A typical PMUT employs a vibrating diaphragm with a diameter of several hundred micrometers, comprising a structural layer and a thin-film piezoelectric layer [23], [31] covered with top and bottom electrodes, as shown in Figure 2. Leveraging the inverse piezoelectric effect, an in-plane stress induced in the piezoelectric layer creates a strain mismatch between the piezoelectric and silicon layers, driving the diaphragm into vibration to transmit ultrasound. Conversely, a voltage signal can be obtained from the electrodes when receiving the incident pressure.

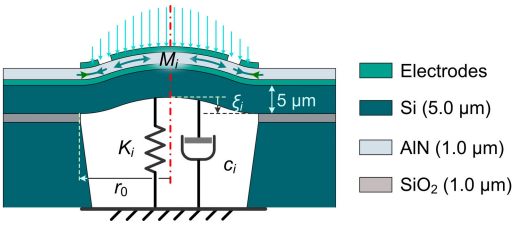

FIGURE 2. **Schematic of a typical PMUT diaphragm with Aluminum Nitride as piezoelectric material.**

1) MODELING OF PLATE VIBRATION

Given that the lateral dimensions of the PMUT significantly exceed its thickness, classic plate theory is employed to model the dynamic behavior of the plate. When the PMUT dynamically receives and transmits pressure waves during operation, the equation of motion of the transversal motion $w(r, t)$ of an axisymmetric fully clamped diaphragm, in polar coordinates, can be expressed as

$$\rho_s \frac{\partial^2 w}{\partial t^2} + c\frac{\partial w}{\partial t} + D_0 \nabla^4 w = q_0(r, t), \tag{1}$$

where $\rho_s = \sum_i \rho_i h_i$ denotes the area plate density of the i-th material layer of the diaphragm, h is the thickness of each material layer, c is the viscous damping coefficient, D_0 denotes the flexural stiffness of the plate, and q_0 represents a transverse force per unit area, encompassing all external loads [31], [32].

Based on the modal analysis method, the solution of Eq. (1) can be presented as a linear combination of the mode shapes $\Psi_i(r)$ [31] assuming

$$w(r, t) = \sum_i^{\infty} \Psi_i \xi_i(t), \tag{2}$$

where $\xi_i(t)$ represents the modal displacements of the diaphragm dependent on time.

Under the axisymmetric harmonic excitation with an angular frequency of $w = 2\pi f$, Ψ_i can be expressed as [31], [33]:

$$\Psi_i = A_0[J_0(\frac{\pi\alpha_i}{r_0}r) - \frac{J_0(\pi\alpha_i)}{I_0(\pi\alpha_i)}I_0(\frac{\pi\alpha_i}{r_0}r)], \tag{3}$$

where $J_0(x)$ and $I_0(x)$ are the zero-order Bessel function of the first kind and the modified Bessel function of the first kind, respectively. Here, r_0 is the radius of the circular-shaped diaphragm, i denotes the number of the radial mode shape, A_0 is the normalization coefficient corresponding to

the position of the reference point on the plate, and α_i fulfills the requirement of [33]

$$I_0(\pi\alpha_i)J_1(\pi\alpha_i) + J_0(\pi\alpha_i)I_1(\pi\alpha_i) = 0. \tag{4}$$

Substituting Eq. (2) into Eq. (1), multiplying each one of them with the corresponding mode shape Ψ_i, and integrated along the radius of the surface of the diaphragm yields

$$M_i\ddot{\xi}_i(t) + c_i\dot{\xi}_i(t) + K_i\xi_i(t) = P_i(t),\ i = 1, 2, 3, \cdots, \tag{5}$$

where the equivalent modal mass M_i, damping c_i, stiffness K_i and the external load P_i of the corresponding vibration modes i can be presented as follows

$$\begin{aligned} M_i &= 2\pi \int_0^{r_0} \rho_s \Psi_i^2\, dr, \\ c_i &= 2\pi \int_0^{r_0} c_i \Psi_i^2\, dr, \\ K_i &= 2\pi \int_0^{r_0} D_0 \frac{d^4\Psi_i}{dr^4} \Psi_i\, dr, \\ P_i &= 2\pi \int_0^{r_0} q_0 \Psi_i\, dr. \end{aligned} \tag{6}$$

In this work, we are utilizing a single vibration mode shape ($i = 1$), ensuring that there is no acoustic energy offset near the surface. This approach is adopted to optimize the system's output efficiency.

2) MODELING OF ACOUSTIC RADIATION

The total radiation impedance of an individual PMUT cell in its 1^{st} vibration mode shape when working in an array can be presented as:

$$Z_i = Z_{ii} + \sum_{j,j\neq i}^{N_{tot}} Z_{ij} \frac{v_j}{v_i}, \tag{7}$$

where v_i and v_j represent the reference velocity of cells i and j, respectively; Z_{ii} denotes the self-radiation impedance of a single PMUT cell, specifically cell i; Z_{ij} stands for the mutual radiation impedance between cells i and j in the array, which has been meticulously analyzed in our previous work [24], [25], [26], [27]. Theoretical modeling and experimental validation have demonstrated that, due to the significantly lower density of air compared to the liquid medium, the acoustic interaction between neighboring cells is exceedingly weak. Each cell exhibits nearly identical dynamic responses when operating individually or within an array under air-coupled conditions [34]. Consequently, in our proposed model for the air-coupled PMUT use case, we simplify Z_{ij} to 0 to expedite calculations. Next, Z_{ii} is calculated based on the Bouwkamp's impedance theorem [35], such as

$$Z_{ii} = \rho_0 c_0 S \frac{(kr_0)^2}{\pi} \int_0^{2\pi} \int_0^{\pi/2+i\infty} D_i^2(\theta, \varphi) \sin\theta\, d\theta\, d\varphi, \tag{8}$$

where ρ_0 and c_0 are the speed of sound and density of the medium respectively, S is the static area of the diaphragm, k is the wave number, and $D_i(\theta, \varphi)$ is the modal directivity of cell i.

3) MODELING OF EQUIVALENT CIRCUIT MODEL

From Eq. (1), the vibration of the PMUT cell can be linearly expressed through two components directly proportional to the loading pressure p_0 and excitation voltage V_0, both of which are encompassed in the variable q_0 [24] such as

$$w_{ref} = Y_m p_0 + b_t V_0, \tag{9}$$

where w_{ref} denotes the displacement of the reference point. In this work, we follow the modeling principles of the established equivalent circuit model through the analogies between electrical voltage and modal force, as well as electrical current and reference velocity, where Y_m is defined as the reference displacement generated by per incident modal force; b_t is the electromechanical admittance defined as the reference displacement generated by per input voltage. The equivalent circuit models for the transmission and receiving mode of each PMUT cell are shown in Figs. 3 (a) and (b), respectively.

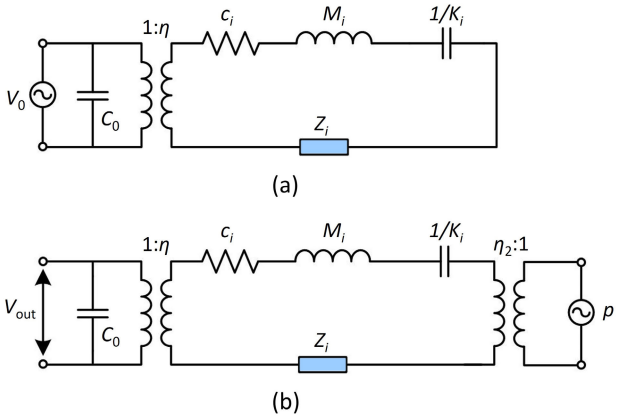

FIGURE 3. Schematic of the equivalent circuit model, (a) Equivalent circuit model for an individual PMUT cell in its transmission mode, where C_0 is the clamped capacitance of the cell, $\eta = b_t/Y_m$ denotes the electromechanical transduction ratio of the PMUT cell, (b) Equivalent circuit model for an individual PMUT cell in its receiving mode, where p is the incident pressure, $\eta_2 = 2\pi \int_0^{r_0} \Psi_i\, dr$.

In the case of a PMUT cell within an air-coupled array, the designed excitation signal or received incident pressure varies across different positions in the array. The dynamic performance of each PMUT cell at different positions within the array can be predicted using the proposed equivalent circuit model, as further elucidated in Section V.

B. FAR FIELD AND ACOUSTIC WAVE PROPAGATION MODELING

1) EXTRACTION OF THE ACOUSTIC BOUNDARY CONDITIONS

In this part, the vibration condition of each PMUT cell will be used as the boundary conditions of the acoustic

domain for the modeling of the acoustic wave propagation. In order to increase the calculation efficiency, the vibration condition of each cell in its 1^{st} vibration mode shape is compared to the vibration of a piston with equivalent radius r_{eq}. Figure 4 (a)-(d) illustrates the error tolerance capacity of equivalent radius for far-field acoustic pressure using four distinct equivalent methods, and all of them are tested in air-coupled working conditions.

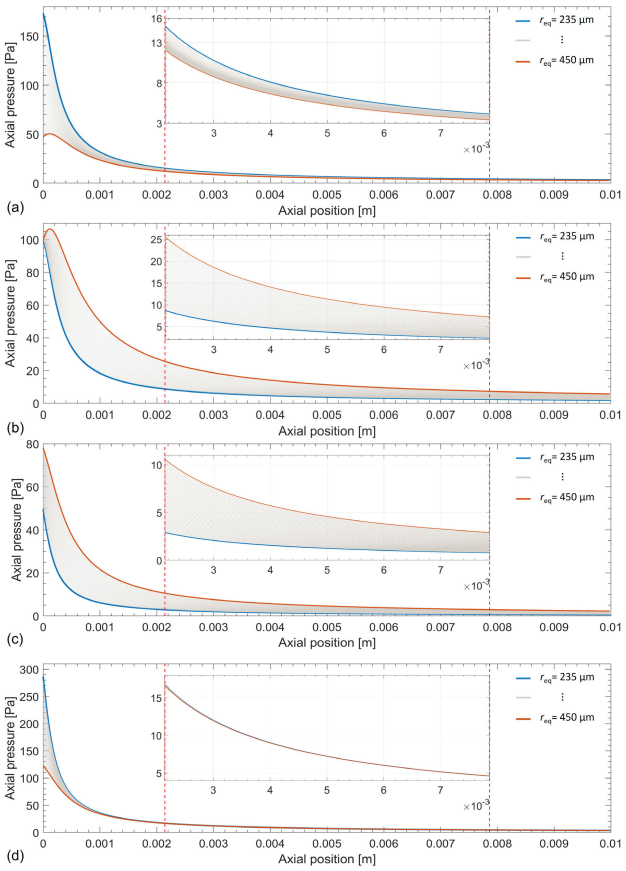

FIGURE 4. Comparison of various equivalence methods for extracting vibration boundary conditions for the acoustic domain, (a) Equivalence method to maintain a consistent incident force, (b) Equivalence method to maintain a consistent average surface pressure, (c) Equivalence method to maintain a consistent vibration velocity, (d) Equivalence method to maintain a consistent volumetric vibration velocity.

In Figure 4 (a), the axial pressure distribution is shown for the PMUT cell with various radius sizes and at the same vibration frequency of 300 kHz, maintaining a constant incidence force of $3\times10^{-5}N$ for each piston model. Figure 4 (b) illustrates axial pressure distribution for the PMUT cell with varied radii, while holding the surface pressure of each piston model constant at 100 Pa. Similarly, Figs. 4 (c) and 4 (d) depict the axial pressure distribution for the PMUT cell with diverse radii, with constant vibration velocity of 0.1 m/s and constant volumetric velocity of 10×10^{-8} m^3/s, respectively.

By comparing the acoustic pressure distribution within the axial range of 2.144 mm to 7.862 mm, corresponding to the Rayleigh distance [36] for circular pistons with radii of 235 μm and 450 μm operating at a frequency of 300 kHz, as depicted in the magnified sections of Figure 4 (a)-(d), it is evident that, despite Figure 4 (a) substantial relative difference in the equivalent radius of up to 90%, the equivalence method maintains a consistent volumetric velocity for each piston model ensures that pistons with varying radii still produce the same output pressure value in the far field. This guarantees the establishment of an equivalent interaction condition between the acoustic wave and the sensing target. Hence, as depicted in Figure 4 (d), adopting the equivalence method to align the vibration boundary of the acoustic domain with the same volumetric velocity as each respective PMUT cell is employed to extract the boundary conditions for the acoustic domain.

2) ACOUSTIC WAVE PROPAGATION SIGNAL MODEL

Having established the necessity of modeling both the interaction between PMUT and the acoustic medium and the extraction of proper acoustic boundary conditions, we now turn our attention to the spatial aspect of ultrasound wave propagation. This involves capturing the directional behavior of sound waves as they propagate through the acoustic media. In the following part of this section, we start with a review of the foundation of ultrasound wave propagation based on ray acoustics. For an excitation signal $p(t)$ in the time domain, the sound pressure $u_0(t)$ after traveling a distance L with the speed of sound as c_0 in an infinite space can be expressed as [37], [38], [39], [40]:

$$u_0(t) = \mathcal{F}^{-1}\{\frac{p(\omega)}{4\pi L}\exp(-j\frac{\omega}{c_0}L)\}, \tag{10}$$

where $\mathcal{F}$ is the Fourier transform and $\mathcal{F}^{-1}$ is its inverse, $p(\omega)$ is the excitation signal in the frequency domain with frequency samples $\omega \in \Omega$ and j is the imaginary unit.

Assuming the presence of a scatter in the space, its received pulse-echo measurements $u(t)$ can be written as

$$u(t) = \mathcal{F}^{-1}\{G(\omega)\frac{p(\omega)}{4\pi LL'}\exp(-j\frac{\omega}{c_0}(L+L')\}, \tag{11}$$

where the frequency-dependent parameter $G(\omega)$ corresponds to the scattering coefficient, L is the length of the transmit path from the transmitter to the scatter, and L' is the length of the receive path from the scatter to the receiver.

Assuming that there are no multiple reflections between scatters, based on (11), for a sensor array of K cells with K different excitation signals $p_k(t)$ for $k \in \{1,\cdots,K\}$ transmitting at the same time, the pulse-echo measurements $u_k(t)$ received by the k-th cell in the array from Q scatterers in the space becomes, i.e.,

$$u_k(t) = \mathcal{F}^{-1}\{\sum_{q=1}^{Q} G_q(\omega)\frac{\exp(-j\frac{\omega}{c_0}L'_{k,q})}{4\pi L'_{k,q}} \times (\sum_{k=1}^{K}\frac{p_k(\omega)}{4\pi L_{k,q}}\exp(-j\frac{\omega}{c_0}L_{k,q})\}, \forall q \in \{1,\cdots,Q\}, \tag{12}$$

where the parameter $G_q(\omega)$ is the scattering coefficient of the q-th scatter, $L_{k,q}$ is the length of the transmit path from the k-th transmitter to the q-th scatter and $L'_{k,q}$ is the length of the receive path from the q-th scatter to the k-th receiver.

IV. COMPRESSED SENSING METHODOLOGY FOR 3D SPATIAL SENSING

As our interest is on reconstructing 3D objects in a 3D spatial ROI, in particular, the main challenge can be narrowed down to the problem of reconstructing any 2D image plane perpendicular to the wave propagation direction, where objects in the 3D ROI can be shown in the stack of a sequence of reconstructed 2D images.

To create the distorted distribution of an acoustic field of the 2D image plane, a multi-frequency PMUT array is proposed in this paper, which is achieved by having different radii of every cell in the array. In addition, the idealized echo signal obtained at each pixel on the image plane should be as least correlated as possible. In this way, the information of a 3D object can be projected onto a set of incoherent basis functions which are constructed by echo signals all image pixels in the ROI.

Dividing the interested image region into M grids, each grid can be considered a potential scatterer. Based on (12), the acoustic signal model in terms of reconstructing the image of the interested spatial region can be derived. Considering that all cells have different transmit signals, the echo signal $a_k^m(t)$ received by the k-th cell from the m-th grid scatterer can be written as $a_k^m(t) = \mathcal{F}^{-1}\{a_k^m(\omega)\}$ with

$$a_k^m(\omega) = \frac{\exp(-j\frac{\omega}{c_0}L'_{k,m})}{4\pi L'_{k,m}} \times \Big(\sum_{k=1}^{K} G_m(\omega)\frac{p_k(\omega)}{4\pi L_{k,m}}\exp(-j\frac{\omega}{c_0}L_{k,m})\Big)\}.$$

Then, echo signals received by all K cells from the scatterer at the m-th grid can be expressed as $\mathbf{a}^m(t) = \sum_{k=1}^{K}\mathcal{F}^{-1}\{\{a_k^m(\omega)\}_{\omega\in\Omega}\}$.

Hence, the dictionary matrix $\mathbf{A}$ constructed by the echo signals of a 2D image region can be written as

$$\mathbf{A} = \Big[\mathbf{a}^1(t), \cdots, \mathbf{a}^m(t), \cdots, \mathbf{a}^M(t)\Big],$$

where the length of each column vector $\mathbf{a}^m(t)$ is determined by the sampling frequency.

Assuming there is an object in the interested image region $\mathbf{x} \in \mathbb{R}^M$, the echo signal collected by every cell is $\mathbf{y}^k(t)$. By summing up echo signals from all cells, the final measurement signal $\mathbf{y}_{echo}(t)$ of the object can be expressed as $\mathbf{y}_{echo}(t) = \sum_{k=1}^{K}\mathbf{y}^k(t)$. Hence, we write the linear signal model to reconstruct image $\mathbf{x}$ from the measurements $\mathbf{y}_{echo}(t)$ as:

$$\mathbf{y}_{echo}(t) = \mathbf{A}\mathbf{x}. \tag{13}$$

Moreover, in the sensor setup, we assume that the positions of cells with different radii are randomly allocated in the PMUT array. However, the correlation between columns of the dictionary matrix $\mathbf{A}$ associated with all pixel grids is not guaranteed to be small. To minimize the correlations between pixel-wise echo signals and to enhance imaging quality, additional information about scatterers can be obtained by rotating the PMUT array. Appending more echo signals obtained by the PMUT array rotation to the signal model (13), the dictionary matrix $\mathbf{A}$ can be extended as

$$\mathbf{A} = \begin{bmatrix} \mathbf{a}_1^1(t) & \cdots & \mathbf{a}_1^m(t) & \cdots & \mathbf{a}_1^M(t) \\ \vdots & & \vdots & & \vdots \\ \mathbf{a}_q^1(t) & \cdots & \mathbf{a}_q^m(t) & \cdots & \mathbf{a}_q^M(t) \\ \vdots & & \vdots & & \vdots \\ \mathbf{a}_Q^1(t) & \cdots & \mathbf{a}_Q^m(t) & \cdots & \mathbf{a}_Q^M(t) \end{bmatrix},$$

where $\mathbf{a}_q^m(t)$ is the echo signal of the scatterer at the m-th grid when the PMUT array is rotated to the q-th angle.

Hence, the final time-domain-based linear signal model of all measurements (including the rotation-based measurements) and the image of the interested region where objects reside becomes:

$$\begin{bmatrix} \mathbf{y}_{\text{echo}}^1 \\ \vdots \\ \mathbf{y}_{\text{echo}}^q \\ \vdots \\ \mathbf{y}_{\text{echo}}^Q \end{bmatrix} = \begin{bmatrix} \mathbf{a}_1^1 & \cdots & \mathbf{a}_1^m & \cdots & \mathbf{a}_1^M \\ \vdots & & \vdots & & \vdots \\ \mathbf{a}_q^1 & \cdots & \mathbf{a}_q^m & \cdots & \mathbf{a}_q^M \\ \vdots & & \vdots & & \vdots \\ \mathbf{a}_Q^1 & \cdots & \mathbf{a}_Q^m & \cdots & \mathbf{a}_Q^M \end{bmatrix} \begin{bmatrix} x_1 \\ \vdots \\ x_m \\ \vdots \\ x_M \end{bmatrix} + \begin{bmatrix} e_1 \\ \vdots \\ e_m \\ \vdots \\ e_M \end{bmatrix},$$

which can be shortly denoted as

$$\mathbf{y} = \mathbf{A}\mathbf{x} + \mathbf{e}, \tag{14}$$

where $\mathbf{y}_{\text{echo}}^q$ is the sum of all echo signals of an object collected by all cells in the PMUT array rotated to the q-th angle, $\mathbf{x}$ is a pixel-wise coefficient vector of the interested image with the object, and $\mathbf{e}$ represents the noises and the nonlinear terms caused by the mismatch between the idealized linear model measurements and actual measurements.

Due to the sparsity nature of having a few objects in the ROI, an estimate of the unknown image $\mathbf{x}$ from measurements $\mathbf{y}$ can be achieved by solving the following optimization problem discussed in compressive sensing, i.e.,

$$\begin{aligned} \min_{x} \quad & \|\mathbf{x}\|_0 \\ \text{s.t.} \quad & \mathbf{y} = \mathbf{A}\mathbf{x} + \mathbf{e}, \end{aligned} \tag{15}$$

where the $\|\mathbf{x}\|_0$ is the number of non-zero entries in $\mathbf{x}$, indicating the positions of pixel-grids occupied by objects.

The most common approaches to solve the problem (15) are ℓ_1-norm optimization methods [41], [42], iterative algorithms [43], [44] and the sparse Bayesian learning strategy [45], [46]. Here we consider the iterative Least Squares (LSQR) algorithm, which is especially suitable for dealing with large-scale sparse systems. By limiting the iterations of LSQR, an estimation can be achieved by tuning a parameter as a trade-off between the reconstructed image resolution and robustness to noises.

V. SIMULATION SETUP AND PLATFORM VALIDATION

In this section, we provide a comprehensive overview of the simulation setup utilized in our studies. This includes simulating acoustic wave propagation within the defined boundaries of a 3D ROI, specifying scatter properties using the k-Wave MATLAB toolbox [28], [29], [30], defining sensor specifications, i.e., cell layout pattern, the radii of PMUT array cells to find out the range of operating center frequency of all cells, and excitation signal.

The k-Wave toolbox is widely used for ultrasound research which can provide accurate and computationally efficient simulation of acoustic wave propagation. It employs a highly effective pseudospectral approach in the scheme with a Fourier collocation spectral method for computing spatial derivatives. The simulation is conducted using MATLAB 2022b combined with CUDA 10.1 and Visual Studio 2017.

A. K-WAVE SETUP

The computational spacing (Δx, Δy, Δz) between grids in the XYZ Cartesian coordinate is 0.25mm. The medium properties are set to be similar to the air (340m/s for the speed of sound, 1.293kg/m^3 for the density). And the acoustic impedance of the scatterer is set to be 218 times greater than that of the medium, ensuring that the scatterer possesses acoustic properties similar to those of a rigid body, while also enhancing the calculation efficiency of the K-wave toolbox [28], [29], [30].

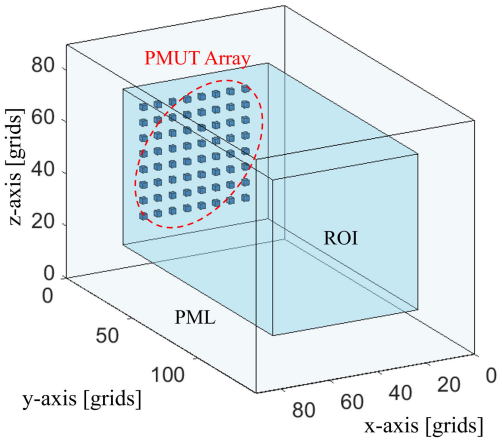

FIGURE 5. Schematic diagram of the 3D acoustic propagation simulation model with a PMUT array layout pattern and 3D ROI.

Every cell is excited by using a time-varying particle velocity as a source. The sensor in receiving mode is set to collect the acoustic pressure reflected from scatters. The simulation schematic and setup parameters are shown in Figure 5 and Table 1.

B. SENSOR ARRAY EXCITATION SETTINGS

The PMUT array used in the proposed simulations has an 8×8 square sensor array composed of 11 types of radius sizes for all the cells, and all the sizes are randomly distributed among 64 cells. cell radius ranges from 235 μm to 350 μm, where the resulting center frequencies range from 505 kHz to 228 kHz correspondingly. A schematic diagram of the cell distribution is shown in Figure 6 (a), and different sizes and colors used in the figure indicate different radii of cells. The bigger the circle is, the larger the radius of the cell is. The excitation signal is a four-cycle flattop windowed tone burst with the center frequency at 360 kHz. Its time domain and frequency domain representation are shown in Figure 6 (b). Then the vibration velocity of each cell based on the equivalent circuit model can be obtained. However, arbitrarily setting different radii of cells in k-Wave is challenging. Based on the discussion in Section III-B1, if two cells with different sizes have the same volumetric velocity at the same location, their spatial distribution of sound pressure is equivalent.

TABLE 1. MATLAB k-Wave toolbox simulation parameters.

Parameter	Unit	Value
Grid definition - $N_x\Delta x$ (Δx)	mm	60 (0.25)
Grid definition - $N_y\Delta y$ (Δy)	mm	114 (0.25)
Grid definition - $N_z\Delta z$ (Δz)	mm	60 (0.25)
Grid definition - PML	mm	15 (0.25)
Acoustic speed of medium	m/s	340
Density of medium	kg/m^3	1.293
Acoustic speed of scatters	m/s	1200
Density of scatters	kg/m^3	80
Attenuation coefficient of medium	dB/MHz/cm	0
Sampling frequency	MHz	25

To realize the cells with different radii in k-Wave, the following steps are carried out in the simulation. Firstly, based on the designed equivalent circuit model, we obtained the vibration velocities of cells with different radii. Then, we converted the calculated vibration velocities into the corresponding vibration velocities of cells having a certain fixed radius with the same volumetric velocity. In this step, all cells have been uniformly set to a size of 0.25×0.25 mm and the pitch size is 1.5 mm. And, based on previous research [47] and our experimental experiences, we tuned the mechanical damping coefficient of the material to ensure that each PMUT cell achieves a −6dB fractional bandwidth distributed in a range from 2% to 5% under the combined effects of mechanical and acoustic damping. The mechanical damping coefficient we set in our equivalent circuit model and the COMSOL time-domain model is equivalent to an isotropic mechanical damping ratio of 0.03 in the COMSOL frequency-domain setting. Figure 6 (c) shows some examples of vibration velocities of cells used in our simulation.

C. SENSOR ARRAY RECEIVING SETTINGS

The PMUT array in our simulation is used for both transmitting and receiving. Compared to traditional transducers, the PMUT sensor has a higher quality factor and better acoustic impedance matching, which can cause a side effect that it may

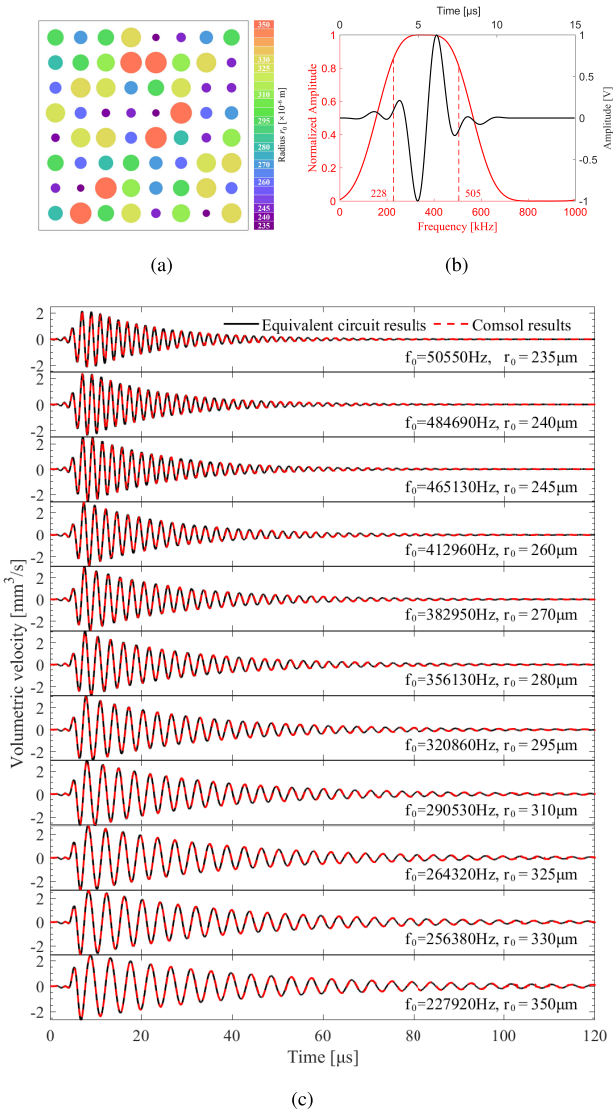

FIGURE 6. PMUT array excitation setting information, (a) Schematic diagram of cell distribution of different radii of PMUT array, (b) 4-cycle flattop windowed tone burst excitation centered at 360 kHz in the time domain and its spectrum of the excitation signal in frequency domain, (c) Comparision of simulated vibration velocities via our proposed equivalent circuit model and COMSOL of some cells shown in the (f_0 is the 1st eigenmode frequency of a cell, r_0 is the radius of a cell).

require a longer time to stop the vibration after the excitation period. In our study, the criterion for vibration cessation is when the vibration amplitude of a cell is less than 10% of its maximum vibration amplitude. Once this criterion is met, all cells are considered in the receiving state. Based on our sensor setup, to have all cells in the receiving states at the same time, 100 μs is chosen as the common vibration cessation time for all the cells. Hence, the minimum detectable distance is 17 mm away from the surface of the PMUT array.

In our simulations, the closest distance is set as 20mm. In k-Wave, each receiving cell collects the acoustic pressure information across the full frequency range. However, the voltage signal of each cell is only sensitive to the information within its frequency response. Using the measurements obtained with the full-frequency acoustic information from k-Wave combined with the receiving equivalent circuit model, the collected acoustic pressure information is transformed into corresponding output voltage signals.

Figure 7 gives an example of the receiving process, where three scatters A, B, and C are placed in the ROI, illustrated in Figure 7 (a), and all cells start transmitting signals at the same time. The echo signal from scatter A is received by cell S16, with the received acoustic pressure information (black line) and the corresponding normalized frequency domain information of its pressure response (red line) shown in Figure 7 (b). Combined with the equivalent circuit model for PMUT reception, the numerically computed output voltage of S16 (black line) and the corresponding COMSOL simulation result (green dashed line) are shown in Figure 7 (c), where the radius of S16 is 260 μm and the corresponding resonant frequency of the voltage signal is 413 kHz. Also, the corresponding normalized FFT transformed computed output voltage signal derived from the equivalent circuit model (red line) is compared with the normalized FFT transformed COMSOL simulated output voltage (black dashed line) in Figure 7 (c). The cell S29 collects the reflected information from scatter B, where its radius is 350 μm and the resonant frequency is 228 kHz. Similarly, its received acoustic pressure information and the corresponding normalized frequency domain information are shown in Figure 7 (d), and the corresponding computed and COMSOL simulated output voltage signals of S29 are depicted in Figure 7 (e), where the resonant frequency of S29 is seen from both the normalized FFT transformed computed output voltage signal and normalized FFT transformed COMSOL simulated output voltage. Lastly, the cell S45 collects the acoustic pressure information from scatter C, and the received acoustic pressure information and the corresponding normalized frequency domain information, with computed and COMSOL simulated output voltage signals and their normalized FFT transforms are shown in Figure 7 (f) and Figure 7 (g), respectively.

VI. VALIDATION AND ANALYSIS OF THE SPATIAL SENSING METHODOLOGY

Constructing an accurate dictionary plays a crucial role in establishing a robust imaging system, which guarantees a high-quality image reconstruction. Therefore, it is essential to know the entire spatial and temporal acoustic field distribution. The dictionary matrix in Eq. (14) can be established either via an accurate numerical model of sound wave propagation or by placing individual scatters in space to collect pulse-echo measurements. In this study, the latter option was chosen. More detailedly, the pulse-echo responses of an interested region are measured by going through every individual scatter placed in every grid of the interested region, where the size of a scatter defined in our experiment is set as 0.5×0.5mm. This procedure is performed only once and is unique for a specific PMUT array. After completing

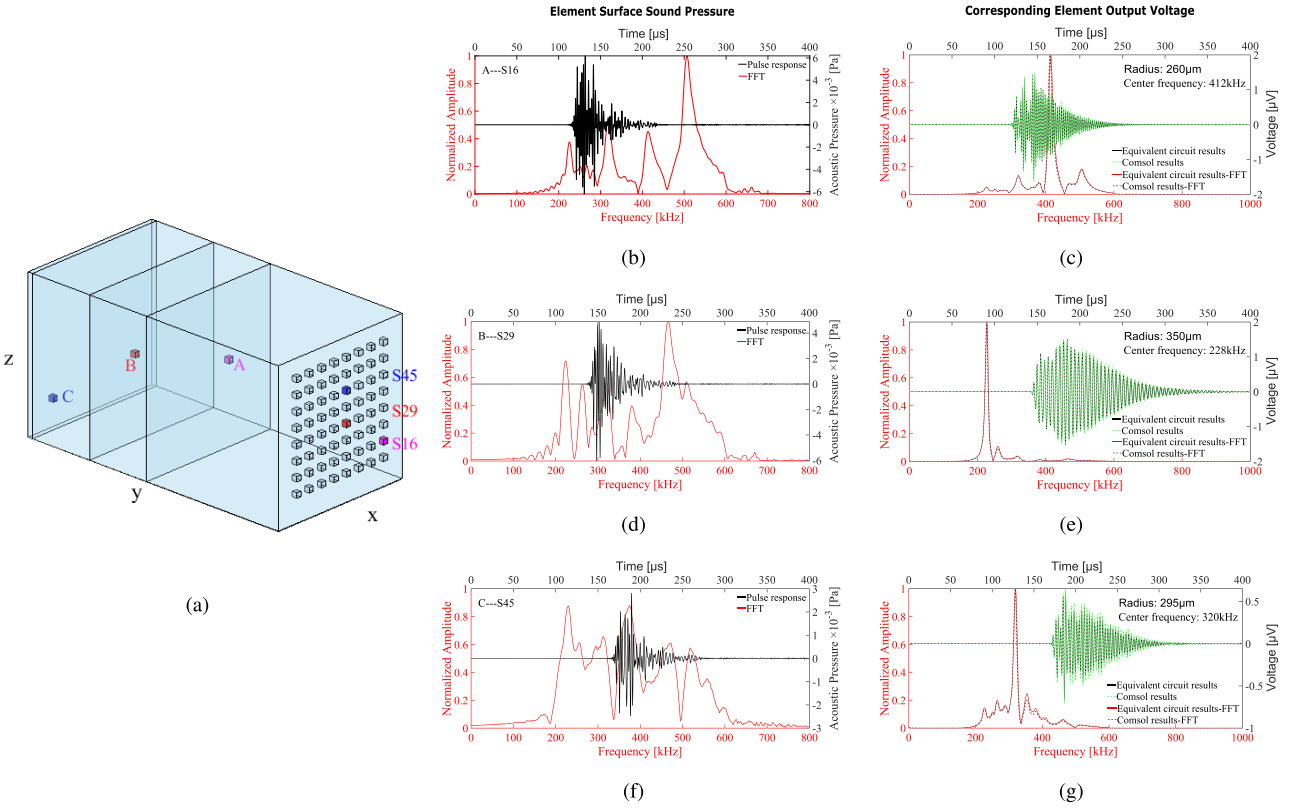

FIGURE 7. PMUT array receiving information, (a) The schematic diagram of 3D ultrasonic propagation model, (b) The acoustic pressure information collected by cell S16 from the ultrasound waves reflected by scatter A (black line) and the corresponding normalized FFT transformed sound pressure signal (red line), (c) The comparison between computed output voltage signal (black line) and COMSOL simulated output voltage signal (green line) of cell S16 and the comparison between the normalized FFT transformed computed output voltage signal derived from the equivalent circuit model (red line) and the COMSOL simulation (black dashed line), (d) The acoustic pressure information collected by cell S29 from the ultrasound waves reflected by scatter B (black line) and the corresponding normalized FFT transformed sound pressure signal (red line), (e) The comparison between computed output voltage signal (black line) and COMSOL simulated output voltage signal (green line) of cell S29 and the comparison between the normalized FFT transformed computed output voltage signal derived from the equivalent circuit model (red line) and the COMSOL simulation (black dashed line), (f) The acoustic pressure information collected by cell S45 from the ultrasound waves reflected by scatter C (black line) and the corresponding normalized FFT transformed sound pressure signal (red line), (g) The corresponding output voltage signal (black line) and COMSOL simulated output voltage signal (green line) of cell S45 and the comparison between the normalized FFT transformed computed output voltage signal derived from the equivalent circuit model (red line) and the COMSOL simulation (black dashed line).

the construction of the pulse-echo dictionary, the following simulation experiments are conducted to verify the proposed method.

A. 2D ULTRASOUND IMAGING RESULTS

In this section, the fundamental principles and techniques for imaging the 2D object are evaluated, and the foundation for understanding image capture and reconstruction is outlined. The 2D ROI is defined as an image plane with 12.5 mm by 12.5 mm located 24 mm away from the PMUT array, which is discretized into 25 by 25 pixels. A triangular object and a rectangular object are placed separately in the ROI. The acoustic impedances of both objects are set to be 218 times more than the acoustic impedance of the air. Then the imaging results under the rotation of the PMUT array either at a single angle (at 0°) or four angles (at 0°, 90°, 180°, and 270°) are shown in Figure 8. The ground-truth location and shape of the object are drawn in each plot (red dashed line) and the reconstructed object is shown in the shaded colored area for comparison. To clearly illustrate the detected area, the amplitudes of all pixels in each picture are normalized with respect to the maximum amplitude value of the reconstructed image.

B. 3D ULTRASOUND IMAGING RESULTS

Building upon the 2D object imaging, in this section, we further explore the complexities of imaging 3D objects. Here, we have used the same simulation setup but with two objects introduced in a 3D space for testing the proposed method with 3D ultrasound imaging. A rectangle is located 20 mm away from the PMUT array, and a triangle is located at a depth of 28 mm away. Dictionary A is composed of echo signals

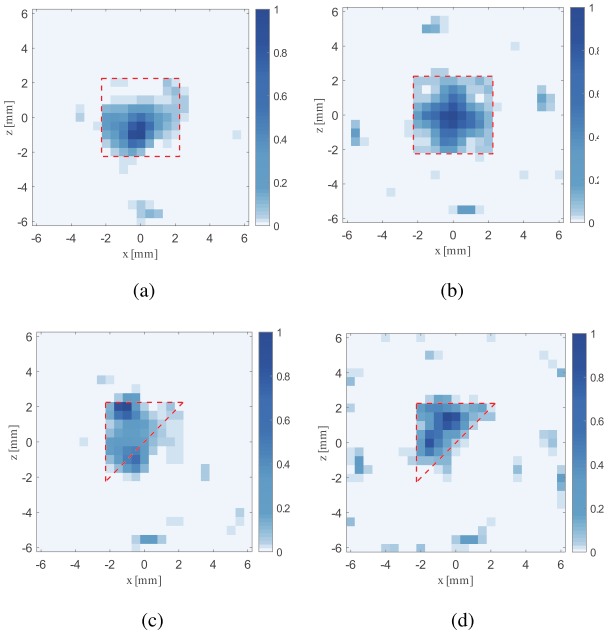

FIGURE 8. 2D image reconstruction results via LSQR, (a) Reconstructed image of a rectangle obtained without rotation, (b) Reconstructed image of the rectangle from measurements obtained with additional 3 rotations of the PMUT array, (c) Reconstructed image of a triangle obtained without rotation, (d) Reconstructed image of the triangle from measurements obtained with additional 3 rotations of the PMUT array.

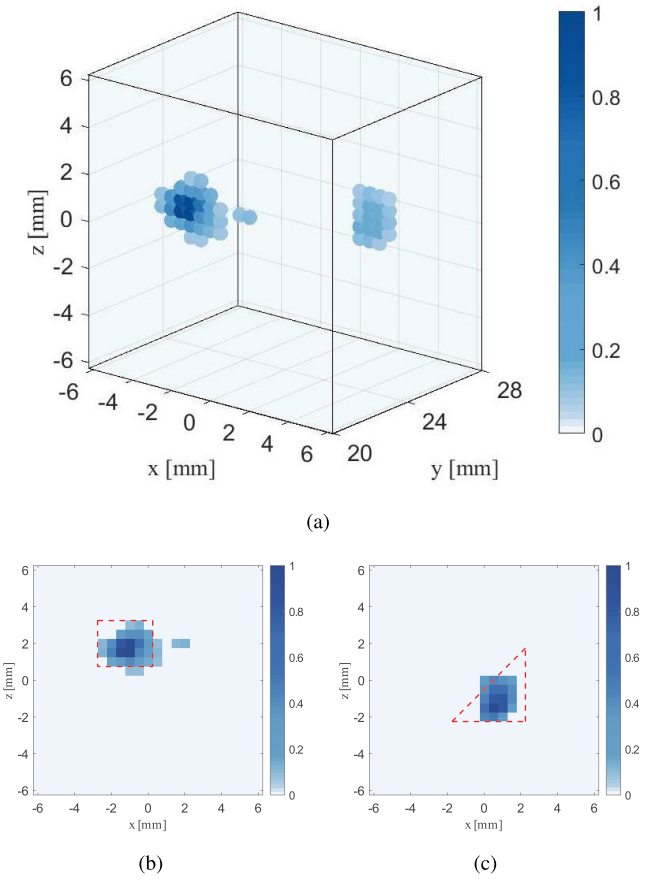

FIGURE 9. 3D image reconstruction results without rotation via LSQR, (a) 3D reconstruction image obtained without rotation, (b) and (c) are the corresponding image slices at depth 20 mm and 28 mm, respectively.

from individual scatters in ROI (from depth 20 mm to 28 mm in the *y*-axis, and 12.5 mm by 12.5 mm for the *xz*-image plane). This scenario consists of the collected information from scatters in every *xz*-image plane at depths of 20, 22, 24, 26, and 28 mm away from the PMUT array. The properties of the detected object are set the same as defined in the 2D imaging scenario. Figure 9 shows the results obtained without rotating the PMUT while the slices of the reconstructed object at depths 20 mm and 28 mm are shown in Figure 9 (b) and (c), respectively. The imaging results obtained by concatenating measurements from all 4 rotation angles of the PMUT array (at 0°, 90°, 180°, 270°) are shown in Figure 10. Similarly, two image slices of objects at depths 20 mm and 28 mm are shown in Figure 10 (b) and (c), respectively.

From all results, shapes of objects can be well sketched in the reconstructed image from measurements obtained from the PMUT array at 4 rotation angles (at 0°, 90°, 180°, and 270°). The imaging results nearly overlap with the real outline as shown in all figures with red dash lines. While in the imaging results without rotation, it is only possible to detect the positions of objects but cannot clearly illustrate their shapes. Based on the results, it is clear that the image reconstruction quality with 4 sets of measurements obtained by rotating the PMUT array is superior to image reconstruction quality without rotation. The reason behind that could be given as follows, by rotating the PMUT array, dictionary matrix **A** is constructed based on measurements at multiple angles. It will reduce the correlation between atoms in the dictionary. Ideally, all atoms in the dictionary matrix should be nearly mutually uncorrelated. Hence, the echo signal from the target object can be uniquely decomposed as a linear combination of individual atoms in the dictionary matrix, in this case, every pixel in an image plane can be distinguished from each other. Moreover, more distinctive object information can be obtained to describe the shape of the object.

C. IMAGE RECONSTRUCTION RESULT ANALYSIS

As shown in Figure 8 and Figure 10, rotating the PMUT array can achieve better imaging performance, and can more precisely detect the positions and outline shapes of the object. To investigate the relationship between correlations and imaging performance, we compute the correlation between atoms within the dictionary matrix **A** constructed with different numbers of rotations in the region at a fixed depth of

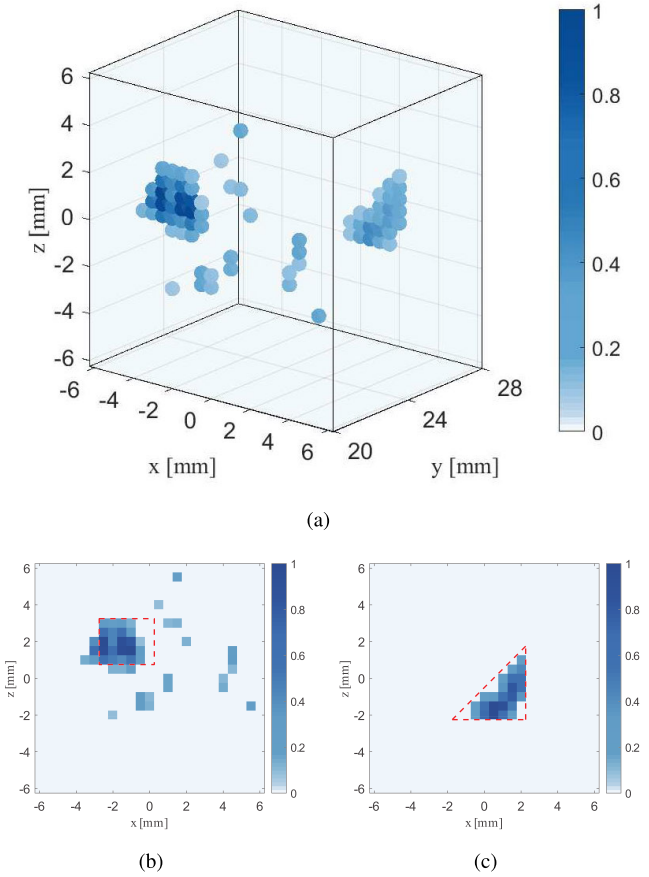

FIGURE 10. 3D image reconstruction results with additional measurements from 3 rotations via LSQR, (a) 3D reconstruction image from measurements obtained with 3 additional rotations of the PMUT array, (b) and (c) are corresponding image slices at depths 20 mm and 28 mm, respectively.

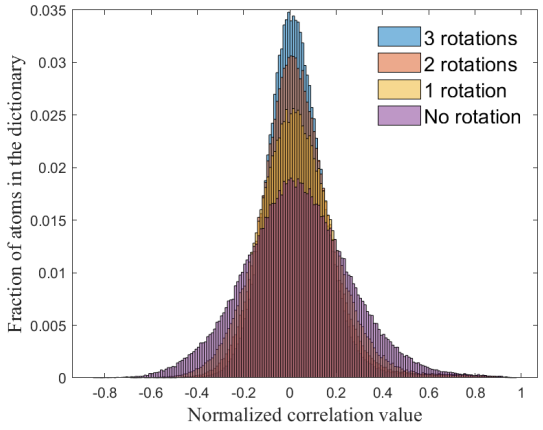

FIGURE 11. Histogram of correlations between atoms within the dictionary matrix constructed with measurements obtained with different numbers of rotations of PMUT array.

24 mm away from the PMUT array. Figure 11 shows the histogram of atomic correlation in the dictionary with different numbers of rotations. The correlation between column

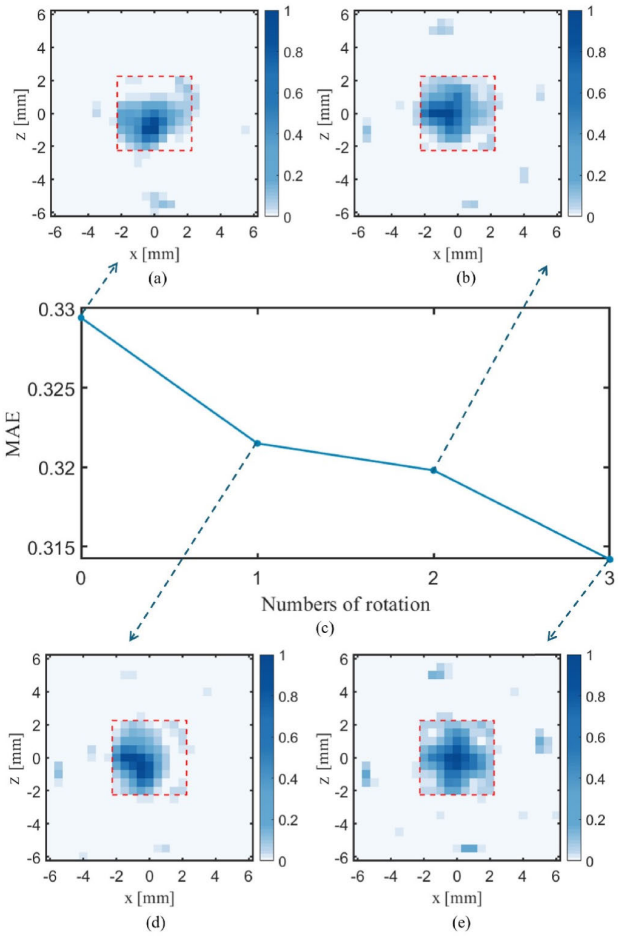

FIGURE 12. Analysis of rotation impact on image reconstruction quality, (a) Image reconstruction of the rectangular from measurements without rotation, (b) Image reconstruction of the rectangular with measurements obtained from additional one rotation, (c) MAE values of the reconstructed rectangular image and the ground-truth image as the rotation number increases, (c) Image reconstruction of the rectangular with measurements obtained from additional two rotations, (d) Image reconstruction of the rectangular with measurements obtained from additional three rotations.

vectors $\mathbf{a^i}$ and $\mathbf{a^j}$ in $\mathbf{A}$ is defined as:

$$\rho_{\mathbf{a^i},\mathbf{a^j}} = \frac{\mathrm{Cov}(\mathbf{a^i},\mathbf{a^j})}{\sqrt{\mathrm{D}(\mathbf{a^i})\mathrm{D}(\mathbf{a^j})}} \quad \forall i,\ j \in \{1,\cdots,M\},$$

where $\mathrm{D}(\mathbf{a^i})$ and $\mathrm{D}(\mathbf{a^j})$ are the corresponding standard deviations of $\mathbf{a^j}$ and $\mathbf{a^j}$, respectively, and $\mathrm{Cov}(\mathbf{a^i},\mathbf{a^j})$ denotes the covariance of $\mathbf{a^i}$ and $\mathbf{a^j}$.

We use the 2D imaging results to demonstrate the impact of the rotation on the image reconstruction quality. To have a qualitative comparison, we employ mean absolute error (MAE), defined as follows, to compare the reconstructed image quality with different rotations,

$$MAE = \frac{1}{M}\sum_{i}^{M} |x_i - \hat{x}_i| \ \forall\ i \in \{1,\cdots,M\},$$

where M is the total number of pixel-wise scatters in the imaging area, $\mathbf{x}$ is the ground-truth image and $\hat{\mathbf{x}}$ is the reconstructed image via any reconstruction algorithms.

The corresponding MAE metric values of reconstructed images of a rectangular with different rotations are provided in Figure 12. Based on the imaging results, we can observe that as the number of rotations increases, the imaging quality continuously improves. This result can be explained from the aspect of the mutual correlation property of the dictionary matrix. Adding more measurements through the PMUT array rotations leads to a narrower distribution of correlations toward zero. The atoms in the dictionary matrix become more orthogonal to each other, which removes ambiguities and increases the resolvability of scatters to improve the image quality.

VII. CONCLUSION

This paper presented a 3D spatial sensing method by using a single-channel air-coupled PMUT with multi-frequency. The presented compressive sensing method not only achieved the localization of objects in 3D space but also demonstrated the capability of this new sensing method for describing the shapes of 2D/3D objects. The proposed approach conducted in simulations has been verified through the 2D/3D image reconstruction to show its effectiveness and robustness for object spatial sensing. The contributions of this work can be summarized as follows:

- The proposed method reconstructs object localization and feature description without the need for pixel-wise scanning, significantly reducing data volume and measurement acquisition time compared to traditional methods. Moreover, the control circuit with a single channel simplifies hardware complexity and reduces the total cost of the sensing system for air-coupled 3D spatial sensing applications;
- Compared to the 3D imaging method based on a coding mask, the proposed method utilizes the usage of a PMUT array which has excellent acoustic impedance matching between the sensor and air-coupling and avoids unnecessary reflections caused by the coding mask, which can improve energy transmission efficiency;
- The established PMUT array simulation platform has significantly improved the efficiency of time domain simulation and built up a foundation for the succeeding system optimization and the application studies of PMUT.
- Lastly, we have observed that the reconstruction results through increased rotation-based measurements allow a clearer delineation of the object's shapes. However, the results exhibit a higher level of noise compared to the non-rotation results. These imaging artifacts have also been observed in [22].

Therefore, we will continue to explore the relationship between the signal-to-noise ratio of reconstructed images and the number of rotations in the future. It is an important and interesting aspect that our future work will focus on.

REFERENCES

[1] Z. Su, L. Ye, and Y. Lu, "Guided Lamb waves for identification of damage in composite structures: A review," *J. Sound Vib.*, vol. 295, nos. 3–5, pp. 753–780, Aug. 2006, doi: 10.1016/j.jsv.2006.01.020.

[2] N. Zhang, M. Zhai, L. Zeng, L. Huang, and J. Lin, "Damage assessment using the Lamb wave factorization method," *Mech. Syst. Signal Process.*, vol. 190, May 2023, Art. no. 110128, doi: 10.1016/j.ymssp.2023.110128.

[3] W. Lee and Y. Roh, "Ultrasonic transducers for medical diagnostic imaging," *Biomed. Eng. Lett.*, vol. 7, no. 2, pp. 91–97, May 2017, doi: 10.1007/s13534-017-0021-8.

[4] A. Marks, D. Patel, T. Sundaram, J. Johnson, and M. Gottlieb, "Ultrasound for the diagnosis of necrotizing fasciitis: A systematic review of the literature," *Amer. J. Emergency Med.*, vol. 65, pp. 31–35, Mar. 2023, doi: 10.1016/j.ajem.2022.12.037.

[5] J. Matsumoto et al., "Acoustic camera system for measuring ultrasound communication in mice," *iScience*, vol. 25, no. 8, Aug. 2022, Art. no. 104812, doi: 10.1016/j.isci.2022.104812.

[6] D. Black, M. Nogami, and S. Salcudean, "Mixed reality human teleoperation with device-agnostic remote ultrasound: Communication and user interaction," *Comput. Graph.*, vol. 118, pp. 184–193, Feb. 2024, doi: 10.1016/j.cag.2024.01.003.

[7] C. H. Wang, J. T. Rose, and F.-K. Chang, "A synthetic time-reversal imaging method for structural health monitoring," *Smart Mater. Struct.*, vol. 13, no. 2, pp. 415–423, Mar. 2004, doi: 10.1088/0964-1726/13/2/020.

[8] G. Matrone, A. S. Savoia, G. Caliano, and G. Magenes, "Ultrasound plane-wave imaging with delay multiply and sum beamforming and coherent compounding," in *Proc. 38th Annu. Int. Conf. IEEE Eng. Med. Biol. Soc. (EMBC)*, Orlando, FL, USA, Aug. 2016, pp. 3223–3226, doi: 10.1109/EMBC.2016.7591415.

[9] V. Perrot, M. Polichetti, F. Varray, and D. Garcia, "So you think you can DAS? A viewpoint on delay-and-sum beamforming," *Ultrasonics*, vol. 111, Mar. 2021, Art. no. 106309, doi: 10.1016/j.ultras.2020.106309.

[10] X. Li, G. Yang, and Y. Gu, "Simulation analysis of MUSIC algorithm of array signal proccessing DOA," in *Proc. Int. Conf. Autom. Control Artif. Intell. (ACAI)*, Mar. 2012, pp. 1838–1841, doi: 10.1049/cp.2012.1349.

[11] X. Yang et al., "Ameliorated-multiple signal classification (Am-MUSIC) for damage imaging using a sparse sensor network," *Mech. Syst. Signal Process.*, vol. 163, Jan. 2022, Art. no. 108154, doi: 10.1016/j.ymssp.2021.108154.

[12] P. Sahuguet, A. Chouippe, and V. Gibiat, "Biological tissues imaging with time domain topological energy," *Phys. Proc.*, vol. 3, no. 1, pp. 677–683, Jan. 2010, doi: 10.1016/j.phpro.2010.01.085.

[13] N. Dominguez, V. Gibiat, and Y. Esquerre, "Time domain topological gradient and time reversal analogy: An inverse method for ultrasonic target detection," *Wave Motion*, vol. 42, no. 1, pp. 31–52, Jun. 2005, doi: 10.1016/j.wavemoti.2004.09.005.

[14] C. Liu, C. Xue, B. Zhang, G. Zhang, and C. He, "The application of an ultrasound tomography algorithm in a novel ring 3D ultrasound imaging system," *Sensors*, vol. 18, no. 5, p. 1332, Apr. 2018, doi: 10.3390/s18051332.

[15] Y. Lu, H.-Y. Tang, S. Fung, B. E. Boser, and D. A. Horsley, "Pulse-echo ultrasound imaging using an AlN piezoelectric micromachined ultrasonic transducer array with transmit beam-forming," *J. Microelectromech. Syst.*, vol. 25, no. 1, pp. 179–187, Feb. 2016, doi: 10.1109/JMEMS.2015.2503336.

[16] D. L. Donoho, "Compressed sensing," *IEEE Trans. Inf. Theory*, vol. 52, no. 4, pp. 1289–1306, Apr. 2006, doi: 10.1109/TIT.2006.871582.

[17] E. J. Candes and M. B. Wakin, "An introduction to compressive sampling," *IEEE Signal Process. Mag.*, vol. 25, no. 2, pp. 21–30, Mar. 2008, doi: 10.1109/MSP.2007.914731.

[18] Z. Gao, L. Dai, S. Han, C. I, Z. Wang, and L. Hanzo, "Compressive sensing techniques for next-generation wireless communications," *IEEE Wireless Commun.*, vol. 25, no. 3, pp. 144–153, Jun. 2018, doi: 10.1109/MWC.2017.1700147.

[19] M. Lustig, D. Donoho, and J. M. Pauly, "Sparse MRI: The application of compressed sensing for rapid MR imaging," *Magn. Reson. Med.*, vol. 58, no. 6, pp. 1182–1195, 2007, doi: 10.1002/mrm.21391.

[20] F. J. Herrmann, M. P. Friedlander, and O. Yilmaz, "Fighting the curse of dimensionality: Compressive sensing in exploration seismology," *IEEE Signal Process. Mag.*, vol. 29, no. 3, pp. 88–100, May 2012, doi: 10.1109/MSP.2012.2185859.

[21] M. F. Duarte et al., "Single-pixel imaging via compressive sampling," *IEEE Signal Process. Mag.*, vol. 25, no. 2, pp. 83–91, Mar. 2008, doi: 10.1109/MSP.2007.914730.

[22] P. Kruizinga et al., "Compressive 3D ultrasound imaging using a single sensor," *Sci. Adv.*, vol. 3, no. 12, Dec. 2017, doi: 10.1126/sciadv.1701423.

[23] J. Jung, S. Kim, W. Lee, and H. Choi, "Fabrication of a two-dimensional piezoelectric micromachined ultrasonic transducer array using a top-crossover-to-bottom structure and metal bridge connections," *J. Micromech. Microeng.*, vol. 23, no. 12, Dec. 2013, Art. no. 125037, doi: 10.1088/0960-1317/23/12/125037.

[24] T. Xu et al., "An analytical equivalent circuit model for optimization design of a broadband piezoelectric micromachined ultrasonic transducer with an annular diaphragm," *IEEE Trans. Ultrason., Ferroelectr., Freq. Control*, vol. 66, no. 11, pp. 1760–1776, Nov. 2019, doi: 10.1109/TUFFC.2019.2928147.

[25] T. Xu et al., "Array design of piezoelectric micromachined ultrasonic transducers with low-crosstalk and high-emission performance," *IEEE Trans. Ultrason., Ferroelectr., Freq. Control*, vol. 67, no. 4, pp. 789–800, Apr. 2020, doi: 10.1109/TUFFC.2019.2956181.

[26] T. Xu et al., "Equivalent circuit models of cell and array for resonant cavity-based piezoelectric micromachined ultrasonic transducer," *IEEE Trans. Ultrason., Ferroelectr., Freq. Control*, vol. 67, no. 10, pp. 2103–2118, Oct. 2020, doi: 10.1109/TUFFC.2020.2993805.

[27] T. Xu et al., "Equivalent circuit model for a large array of coupled piezoelectric micromachined ultrasonic transducers with high emission performance," *IEEE Trans. Ultrason., Ferroelectr., Freq. Control*, vol. 68, no. 3, pp. 718–733, Mar. 2021, doi: 10.1109/TUFFC.2020.3008179.

[28] B. E. Treeby, J. Budisky, E. S. Wise, J. Jaros, and B. T. Cox, "Rapid calculation of acoustic fields from arbitrary continuous-wave sources," *J. Acoust. Soc. Amer.*, vol. 143, no. 1, pp. 529–537, Jan. 2018, doi: 10.1121/1.5021245.

[29] B. E. Treeby and B. T. Cox, "K-wave: MATLAB toolbox for the simulation and reconstruction of photoacoustic wave fields," *J. Biomed. Opt.*, vol. 15, no. 2, 2010, Art. no. 021314, doi: 10.1117/1.3360308.

[30] B. T. Cox et al., "Experimental validation of photoacoustic K-space propagation models," *Proc. SPIE*, vol. 5320, pp. 238–248, Jul. 2004, doi: 10.1117/12.531178.

[31] F. Sammoura, K. Smyth, S.-G. Kim, and L. Lin, "An accurate equivalent circuit for the clamped circular multiple-electrode PMUT with residual stress," in *Proc. IEEE Int. Ultrason. Symp. (IUS)*, Jul. 2013, pp. 275–278, doi: 10.1109/ULTSYM.2013.0071.

[32] K. Smyth, S. Bathurst, F. Sammoura, and S. Kim, "Analytic solution for N-electrode actuated piezoelectric disk with application to piezoelectric micromachined ultrasonic transducers," *IEEE Trans. Ultrason., Ferroelectr., Freq. Control*, vol. 60, no. 8, pp. 1756–1767, Aug. 2013, doi: 10.1109/TUFFC.2013.2756.

[33] W. Thein, "Vibration of circular plates," *J. Acoust. Soc. Amer.*, vol. 34, no. 3, pp. 275–281, 1962, doi: 10.1121/1.1928110.

[34] X. Chen, J. Xu, H. Ding, X. Liu, D. Chen, and J. Xie, "A high-accuracy in-air reflective rangefinder via PMUTS arrays using multi-frequency continuous waves," in *Proc. 20th Int. Conf. Solid-State Sensors, Actuat. Microsystems Eurosensors XXXIII (TRANSDUCERS EUROSENSORS XXXIII)*, Jun. 2019, pp. 154–157, doi: 10.1109/TRANSDUCERS.2019.8808651.

[35] C. J. Bouwkamp, "A contribution to the theory of acoustic radiation," *J. Acoust. Soc. Amer.*, vol. 34, no. 3, pp. 41–67, 1992.

[36] D. T. Blackstock, "Fundamentals of physical acoustics," *Acoust. Soc. Amer.*, vol. 109, no. 4, pp. 1274–1276, 2001, doi: 10.1121/1.1354982.

[37] P. R. Stepanishen, "Pulsed transmit/receive response of ultrasonic piezoelectric transducers," *J. Acoust. Soc. Amer.*, vol. 69, no. 6, pp. 1815–1827, Jun. 1981, doi: 10.1121/1.385919.

[38] J. A. Jensen, "A model for the propagation and scattering of ultrasound in tissue," *J. Acoust. Soc. Amer.*, vol. 89, no. 1, pp. 182–190, Jan. 1991, doi: 10.1121/1.400497.

[39] J. A. Jensen and N. B. Svendsen, "Calculation of pressure fields from arbitrarily shaped, apodized, and excited ultrasound transducers," *IEEE Trans. Ultrason., Ferroelectr., Freq. Control*, vol. 39, no. 2, pp. 262–267, Mar. 1992, doi: 10.1109/58.139123.

[40] P. van der Meulen, M. Coutino, P. Kruizinga, J. G. Bosch, and G. Leus, "Blind calibration for arrays with an aberration layer in ultrasound imaging," in *Proc. 28th Eur. Signal Process. Conf. (EUSIPCO)*, Jan. 2021, pp. 1269–1273, doi: 10.23919/Eusipco47968.2020.9287755.

[41] C.-B. Xu, Z.-B. Yang, X.-F. Chen, S.-H. Tian, and Y. Xie, "A guided wave dispersion compensation method based on compressed sensing," *Mech. Syst. Signal Process.*, vol. 103, pp. 89–104, Mar. 2018, doi: 10.1016/j.ymssp.2017.09.043.

[42] Z. Zhang, L. Zeng, and N. Zhang, "Damage imaging using multipath-scattered Lamb waves under a sparse reconstruction framework," *Struct. Health Monitor.*, Oct. 2023, doi: 10.1177/14759217231203241.

[43] J. A. Tropp, "Greed is good: Algorithmic results for sparse approximation," *IEEE Trans. Inf. Theory*, vol. 50, no. 10, pp. 2231–2242, Oct. 2004, doi: 10.1109/TIT.2004.834793.

[44] H. Li, L. Wang, X. Zhan, and D. K. Jain, "On the fundamental limit of orthogonal matching pursuit for multiple measurement vector," *IEEE Access*, vol. 7, pp. 48860–48866, 2019, doi: 10.1109/ACCESS.2019.2907684.

[45] S. Ji, Y. Xue, and L. Carin, "Bayesian compressive sensing," *IEEE Trans. Signal Process.*, vol. 56, no. 6, pp. 2346–2356, Jun. 2008, doi: 10.1109/TSP.2007.914345.

[46] H. Zhang, J. Hua, F. Gao, and J. Lin, "Efficient Lamb-wave based damage imaging using multiple sparse Bayesian learning in composite laminates," *NDT E Int.*, vol. 116, Dec. 2020, Art. no. 102277, doi: 10.1016/j.ndteint.2020.102277.

[47] F. Sammoura, S. Shelton, S. Akhbari, D. Horsley, and L. Lin, "A two-port piezoelectric micromachined ultrasonic transducer," in *Proc. Joint IEEE Int. Symp. Appl. Ferroelectric, Int. Workshop Acoustic Transduction Mater. Devices Workshop Piezoresponse Force Microsc.*, May 2014, pp. 1–4, doi: 10.1109/ISAF.2014.6923004.

TINGZHONG XU received the bachelor's and Ph.D. degrees in mechanical engineering from Xi'an Jiaotong University, Xi'an, China, in 2013 and 2020, respectively, and the Ph.D. degree in mechanical and manufacturing engineering from The University of New South Wales (UNSW), Australia, in 2021.

Since 2021, he has been a Senior Scientist with Silicon Austria Laboratories (SAL). His research encompasses both hardware (MEMS) and software (signal processing algorithms) aspects of sensing technology. His work involves modeling, designing, fabricating, and characterizing acoustic MEMS, including microphones, PMUTs, and CMUTs. He places particular emphasis on piezoelectric micromachined ultrasonic transducers (PMUTs), exploring their applications in industrial, biomedical, and consumer electronics. Additionally, he actively explores multi-modal sensing technology, advocating for the on-chip integration of MEMS acoustic sensors with multi-physical sensing technology.

ZHONGJIE ZHANG was born in Wuwei, China. He received the bachelor's degree in mechanical design and manufacture and automation from Hunan University, Changsha, China, in 2021. He is currently pursuing the master's degree in mechanical engineering with Xi'an Jiaotong University, Xi'an, China.

In 2023, he joined the Silicon Austria Laboratories (SAL) through the Joint Training Student Program. His research interests include nondestructive testing, ultrasound imaging, and piezoelectric micromachined ultrasonic transducer (PMUT).

RODRIGO TUMOLIN ROCHA was born in Brazil. He received the bachelor's degree in physics from Sao Paulo State University, Rio Claro, Brazil, in 2012, the master's degree from Sao Paulo State University, Bauru, Brazil, in 2014, and the Ph.D. degree from Sao Paulo State University, Brazil, in 2016, working on nonlinear dynamics and vibration-based energy harvesting from ambient vibration. From 2016 to 2018, he was a Post-Doctoral Fellow with the Federal University of Technology Parana (UTFPR), Ponta Grossa, Parana, working on nonlinear dynamics, control, and energy harvesting on macro and microstructures. From 2018 to 2022, he was a Post-Doctoral Fellow with the King Abdullah University of Science and Technology (KAUST), Thuwal, Saudi Arabia, working on modeling and experimental characterization of nonlinear dynamics of compound microstructures. Currently, he is a Senior Scientist with the Piezoelectric Microsystem Technologies, Silicon Austria Laboratories, Austria.

LIANG ZENG was born in Changsha, China. He received the B.S. degree in measurement and control technology and instruments and the M.S. degree in vehicle engineering from Beijing Jiaotong University, Beijing, China, in 2007 and 2009, respectively, and the Ph.D. degree in mechanical engineering from Xi'an Jiaotong University, Xi'an, China, in 2014.

He is currently an Associate Professor with the State Key Laboratory for Manufacturing System Engineering, School of Mechanical Engineering, Xi'an Jiaotong University. His research interests include nondestructive testing, structural health monitoring, and ultrasound imaging.

CHUNLEI XU received the bachelor's degree in applied mathematics from Wuhan University, China, in 2010, and the master's degree in mathematical finance and the Ph.D. degree in management mathematics from the University of Birmingham, U.K., in 2011 and 2016, respectively.

She pursued a post-doctoral research position with the Image and Signal Processing Group (ISPGroup), ICTEAM Institute, UCLouvain, Belgium, from 2016 to 2018. From 2018 to 2021, she was a Research Engineer with the 5G System Automation Group, Nokia, Hungary. She is currently a Senior Scientist with the Silicon Austria Laboratories (SAL), Austria. Her research activities focus on sparse signal representation and other low-complexity signal priors, compressive sensing (theory and applications), inverse problems solving in ultrasound imaging, and machine learning methods for radar and ultrasound sensing applications.